Supplement

Quantification of solid fuel combustion and aqueous chemistry contribution to secondary organic aerosol during wintertime haze events in Beijing

Yandong Tong[1], Veronika Pospisilova[1,a], Lu Qi[1], Jing Duan[2], Yifang Gu[2], Varun Kumar[1], Pragati Rai[1], Giulia Stefenelli[1], Liwei Wang[1], Ying Wang[2], Haobin Zhong[2], Urs Baltensperger[1], Junji Cao[2], Ru-Jin. Huang[2], Andre Stephan Henry Prevot[1], and Jay Gates Slowik[1]

[1]Laboratory of Atmospheric Chemistry, Paul Scherrer Institute (PSI), 5232 Villigen, Switzerland

[2]Key Lab of Aerosol Chemistry & Physics, Institute of Earth Environment, Chinese Academy of Sciences, Xi'an, China

[a]now at: Tofwerk AG, Uttigenstrasse 22, 3600 Thun, Switzerland

Correspondence: J. G. Slowik (jay.slowik@psi.ch)

Text S1: Custom peak fitting algorithm

Due to high pollution levels, significant denuder break-through was observed, increasing the background signal. The high intensity of background ions relative to particle-phase signals compromised our initial attempts at high-resolution fitting. Under these sub-optimal conditions, particle-phase ions, which are typically more oxygenated than the background ions and thus occur at lower mass defect, appeared as small but clearly resolved peaks or shoulders on the leading edge of the background ions (as shown in Fig. S3). However, they could not be fitted well by the standard Tofware fitting algorithm and a custom procedure was therefore employed.

In general, peak fitting is accomplished by minimising the objective function χ^2, shown in Eq. S1:

$$\chi^2 = \Sigma\left(\frac{y-y_i}{w_i}\right)^2 \qquad \text{(S1)}$$

Here y is the fitted value, while y_i and w_i denote the signal and weight at position i on the *m/z* axis. In default Tofware (and IGOR) operation, w_i is simply 1. This results in fitting errors for the (low-intensity) particle-phase signals, because the low signal intensity means that such errors have a negligible effect on χ^2, resulting in a poor fit to this region of the spectrum (see Fig. S3). Here we instead calculate w_i according to Eq. S1 as follows: by applying the minimum error e_i ($w_i = \log_{100}(y_i/e_i) + 1$ if y_i is above or equal to the minimum error, and $w_i = 1$ if y_i is below the minimum error). The weight w_i should always be positive, therefore, when y_i is equal to the minimum error and $\log_{100}(y_i/e_i)$ is equal to 0, we translate w_i to positive by plus 1. When y_i is equal to the minimum error, we set $y_i = e_i$, therefore, $w_i = 1$. Here e_i is an estimation of the baseline, calculated as the averaged baseline value out of integration region. This increases the relative weight of the spectral region containing particle-phase signal, and improves the fits to this region (see Fig. S4). Nevertheless, their low intensity will result in fits with higher uncertainty than normally obtained via EESI-TOF/Tofware data analysis. This fitting algorithm does not significantly affect the fit quality of the high intensity background ions, which are removed from further analysis according to the criteria discussed in Text S2.

Text S2: Selection of ions dominated by particle-phase signal

In the present campaign, ions measured by the EESI-TOF may derive from (1) particle-phase compounds, (2) the working solution and its impurities, and (3) volatile and semi-volatile compounds transmitted to the spray because of denuder breakthrough. Of these sources, (1) and (2) are intrinsic to the EESI-TOF system, while (3) represents a special challenge of the current campaign. However, the combination of these signal sources, especially (3), makes it non-trivial to identify ions arising primarily from particle-phase signal (which are the only ones desirable to retain for further analysis). In fact, the denuder breakthrough issues make a perfect separation between particle and gas signals impossible for semi-volatile compounds, and complicates background subtraction by increasing background intensity and variability. Here we applied the following 3 criteria to select particle-dominated ions for further analysis. Criteria (1) and (2) address signal-to-noise and signal-to-background considerations, respectively, and are similar to those applied in previous EESI-TOF studies (Qi et al., 2019; Stefenelli et al., 2019). However, they were found to be insufficient in the current study due to denuder breakthrough, and therefore a third criterion was added to assess the likelihood of a given ion partitioning to the particle phase:

1. Ratio of signal to uncertainty, M_{diff}/σ_{diff}, where σ_{diff} represents the precision-based uncertainties calculated for PMF analysis (in Section 2.3), which depend primarily on ion counting statistics. Ions with a median of the ratio $M_{diff}/\sigma_{diff} < 0.2$ were removed from further analysis (Paatero and Hopke, 2003).
2. Ratio of signal to background, M_{diff}/M_{filter}. This identifies ions whose time series is dominated by instabilities in the spray and/or background drifts due to adsorption/desorption of semi-volatile compounds. Ions with median of ratio of $M_{diff}/M_{filter} < 0.1$ were removed.
3. Estimation of saturation vapour mass concentration (C_0). saturation mass concentration (C_0) of every ion was estimated according to Eq. S2, which parameterises the C_0 by elemental composition (Li et al., 2016):

$$\log_{10} C_0 = \left(n_C^0 - n_C\right)b_C - n_O b_O - 2n_c n_O/(n_C + n_O)b_{CO} - n_N b_N - n_S b_S \qquad \text{(S2)}$$

   where n_C^0 is the reference carbon number, n_c, n_O, n_N and n_S stand for number of carbon, oxygen, nitrogen and sulphur atoms in the molecules, respectively, b_C, b_O, b_N and b_S are the contribution of each carbon, oxygen, nitrogen and sulphur atom to $\log_{10} C_0$, respectively, and b_{CO} is carbon–oxygen nonideality (Donahue et al., 2011). These values can be found elsewhere (Li et al., 2016). As levoglucosan has been well characterised by Lopez-Hilfiker et al. (2019) and expected to be in the particle phase under the low temperature in winter in China, ions with an estimated C_0 higher than that of levoglucosan were assumed to be dominated by breakthrough of organic vapour and excluded from further analysis. The choice of levoglucosan as a cut-off point means that our results will somewhat underestimate contributions of less oxygenated and lower molecular weight species, as well as small organic acids.

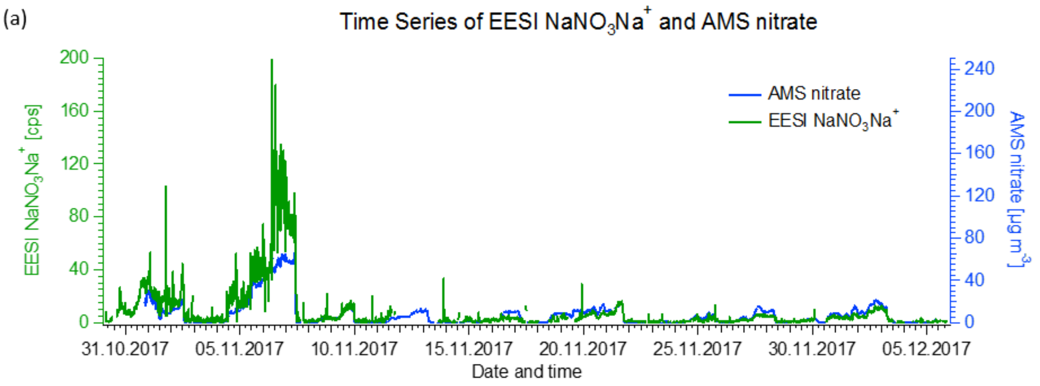
(a)
Time Series of EESI NaNO$_3$Na$^+$ and AMS nitrate
AMS nitrate
EESI NaNO$_3$Na$^+$
EESI NaNO$_3$Na$^+$ [cps]
0
40
80
120
160
200
AMS nitrate [µg m^{-3}]
0
40
80
120
160
200
240
31.10.2017
05.11.2017
10.11.2017
15.11.2017
20.11.2017
25.11.2017
30.11.2017
05.12.2017
Date and time

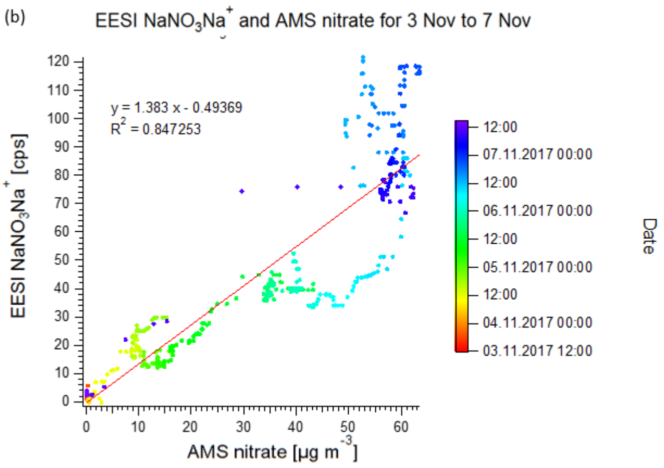
(b)
EESI NaNO$_3$Na$^+$ and AMS nitrate for 3 Nov to 7 Nov
y = 1.383 x - 0.49369
R^2 = 0.847253
EESI NaNO$_3$Na$^+$ [cps]
AMS nitrate [µg m^{-3}]
0
10
20
30
40
50
60
70
80
90
100
110
120
12:00
07.11.2017 00:00
12:00
06.11.2017 00:00
12:00
05.11.2017 00:00
12:00
04.11.2017 00:00
03.11.2017 12:00
Date

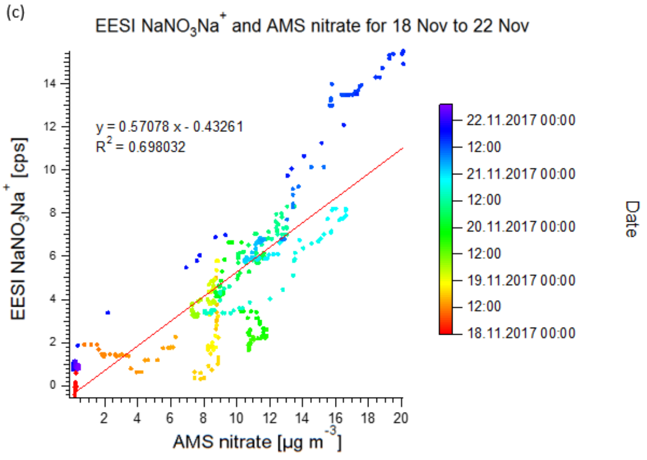
(c)
EESI NaNO$_3$Na$^+$ and AMS nitrate for 18 Nov to 22 Nov
y = 0.57078 x - 0.43261
R^2 = 0.698032
EESI NaNO$_3$Na$^+$ [cps]
AMS nitrate [µg m^{-3}]
0
2
4
6
8
10
12
14
16
18
20
22.11.2017 00:00
12:00
21.11.2017 00:00
12:00
20.11.2017 00:00
12:00
19.11.2017 00:00
12:00
18.11.2017 00:00
Date

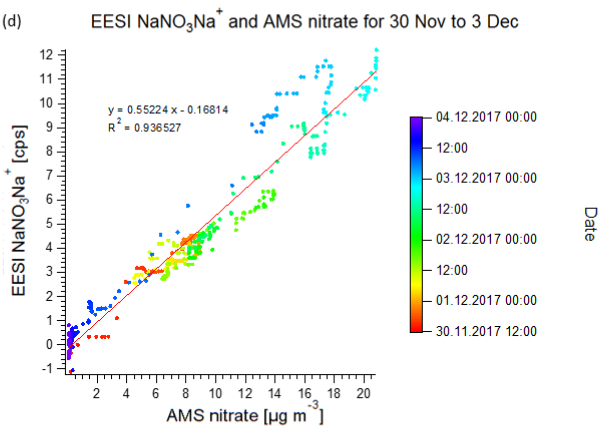

Figure S1. Time series of EESI-TOF Na$_2$NO$_3$ and AMS nitrate are shown in (a), and scatter plots of EESI-TOF Na$_2$NO$_3$ vs AMS nitrate in three different haze events from (b) to (d).

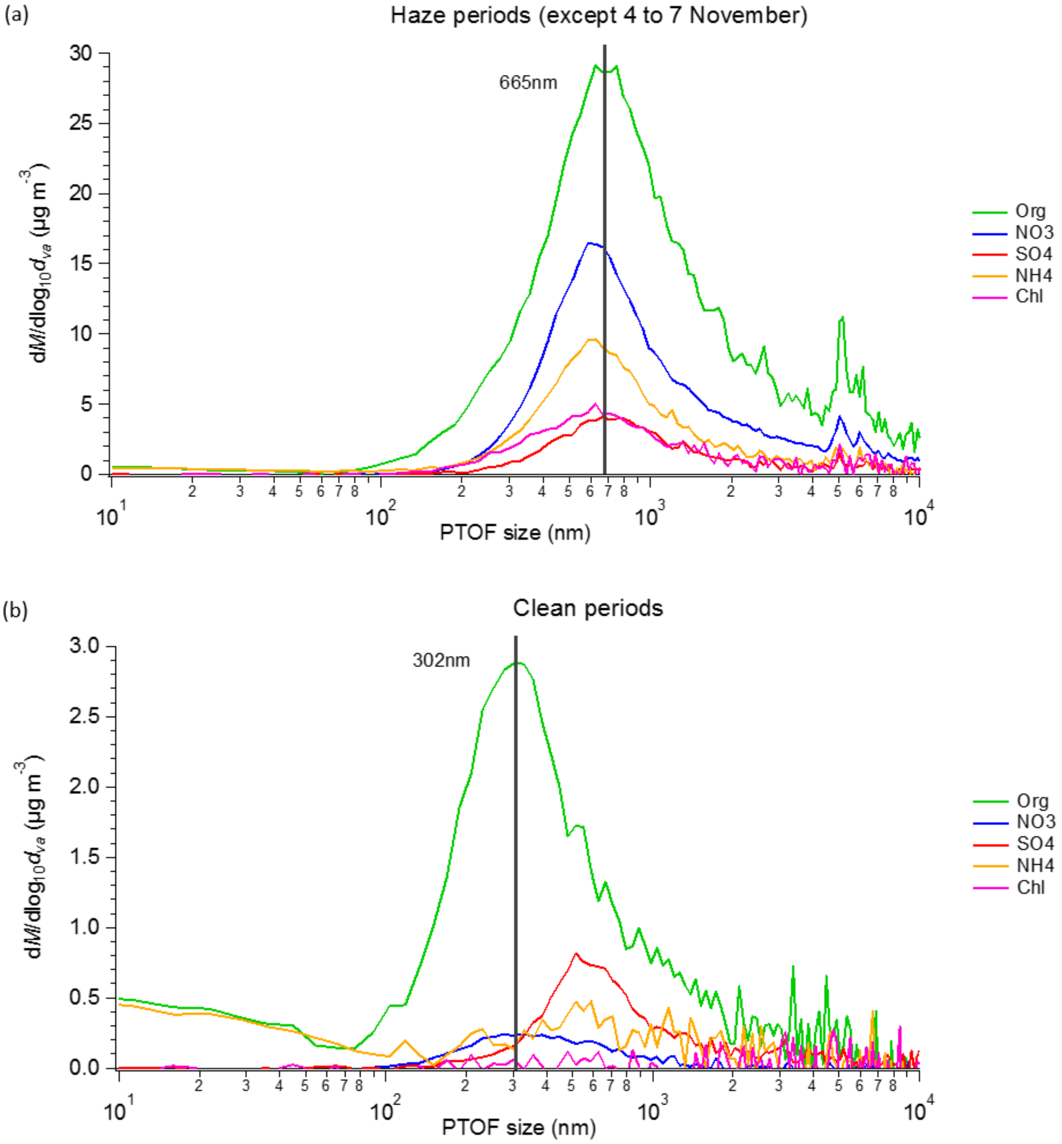

Figure S2. AMS mass distributions averaged over (a) all haze events except the aqueous chemistry-dominated event from 4 to 7 Nov., and (b) all clean periods.

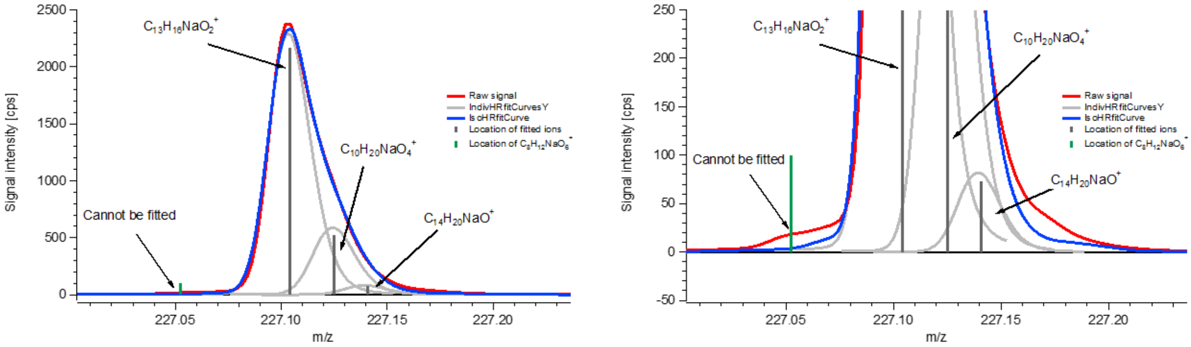

Figure S3. An example of peak fitting issue from the standard Tofware fitting algorithm. The left subplot is original scale and the right subplot is zoomed scale. Red line is the raw signal, blue line is summed fitted peaks, grey lines are the fit for individual ions, and grey sticks are fitted ions. Green stick is the location of $C_8H_{12}O_6Na^+$ (227.052).

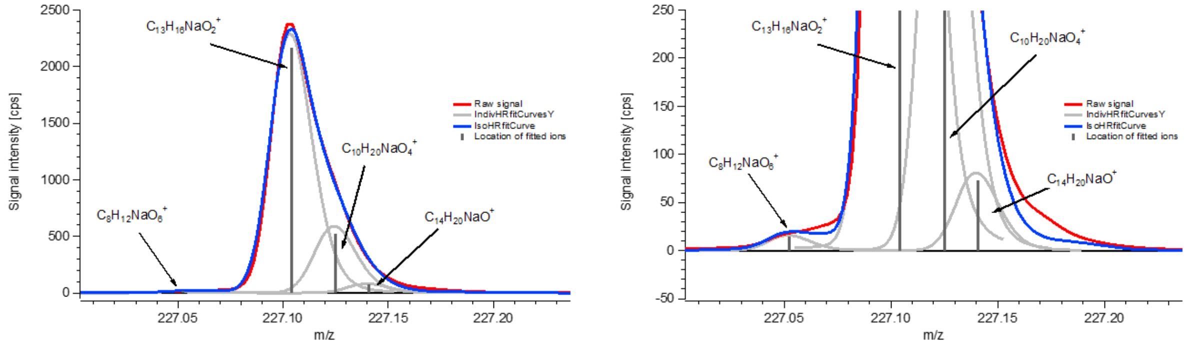

Figure S4. The same example of peak fitting after applying weighting method. The left subplot is original scale and the right subplot is zoomed scale. Red line is the raw signal, blue line is summed fitted peaks, grey lines are the fit for individual ions, and grey sticks are fitted ions. This ion $C_8H_{12}O_6Na^+$ (227.052) is fitted by the revised weighting method. The revised method does not provide a perfect solution to the fitting problem, but significantly decreases the bias.

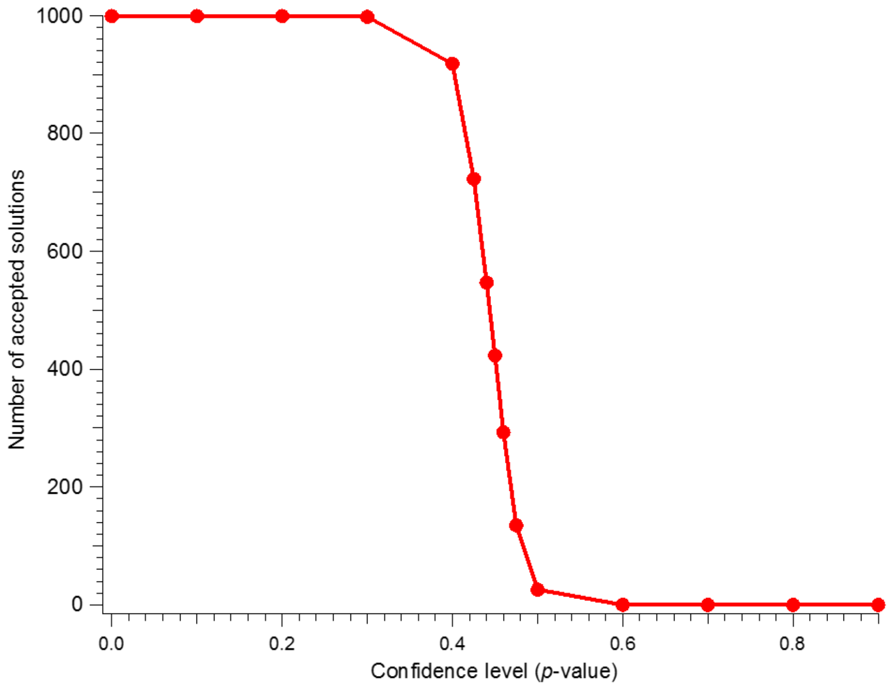

Figure S5. Number of good runs as a function of confidence level (*p* value) in the bootstrap analysis of the eight-factor solution in AMS PMF.

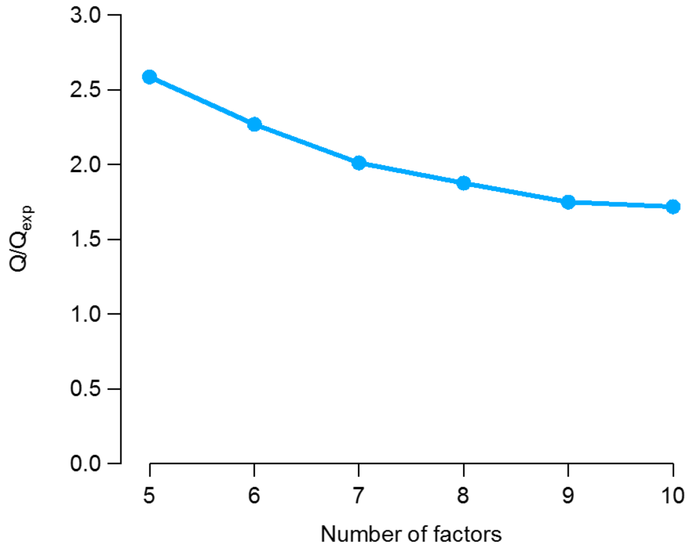

Figure S6. Q/Q_{exp} as a function of number of factors in AMS PMF result.

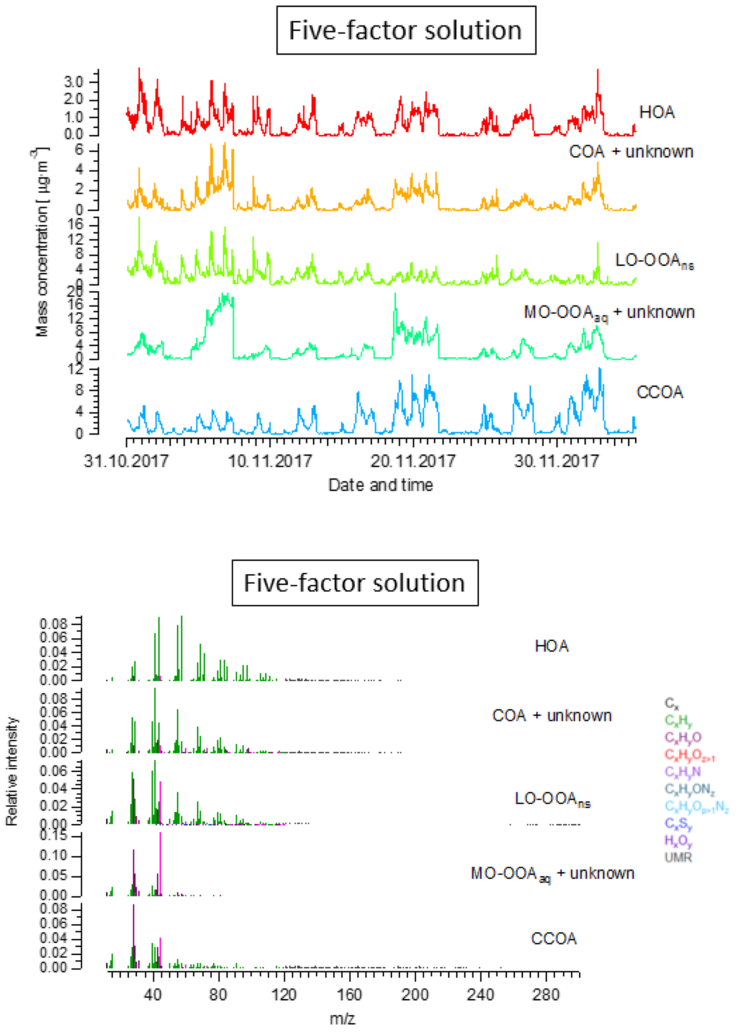

Figure S7. Factor time series and factor profiles of five-factor solution from AMS PMF.

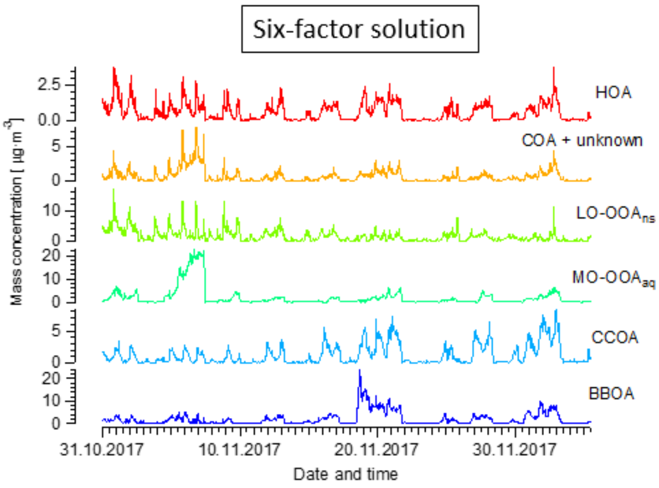

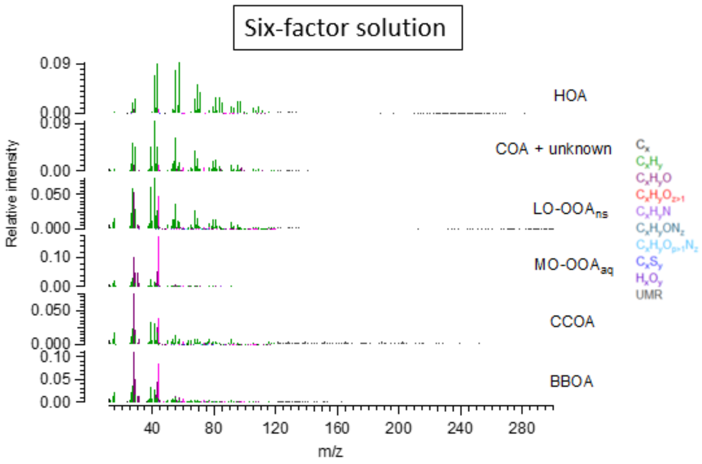

Figure S8. Factor time series and factor profiles of six-factor solution from AMS PMF.

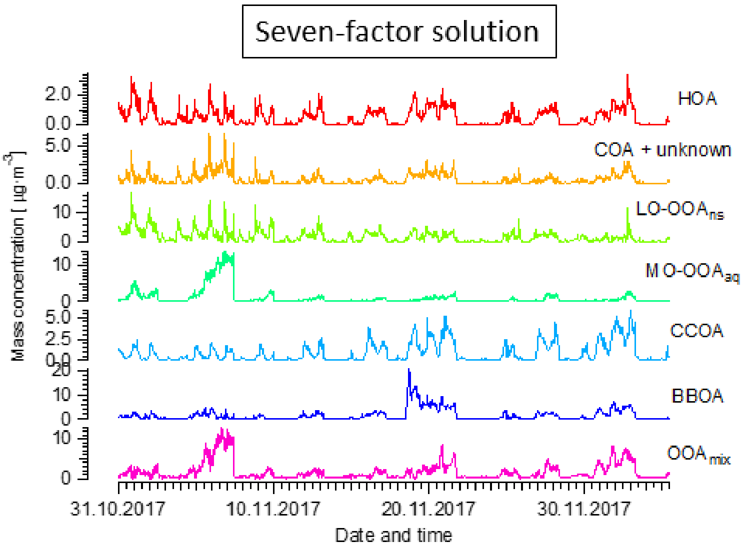

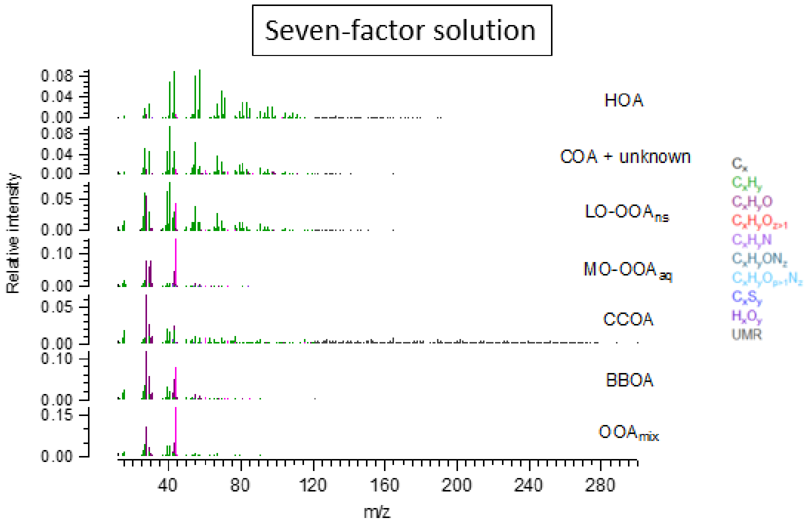

Figure S9. Factor time series and factor profiles of seven-factor solution from AMS PMF

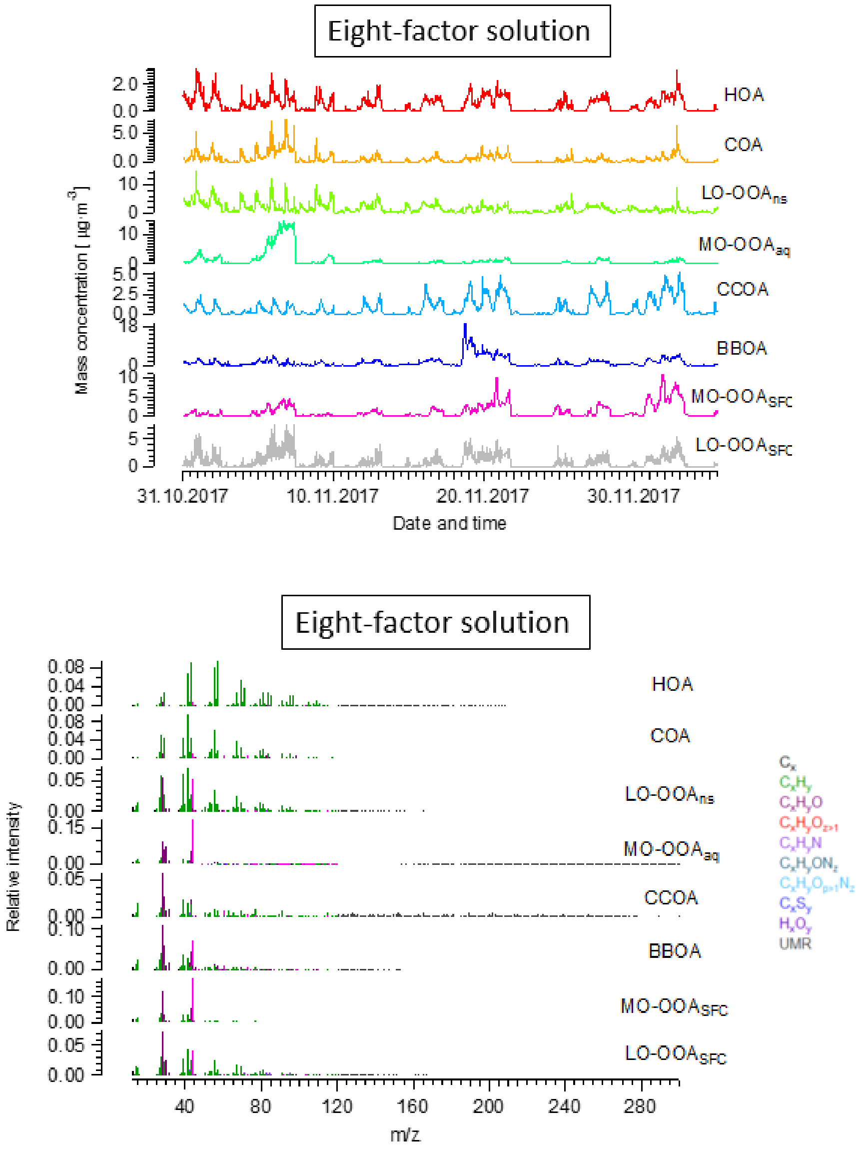

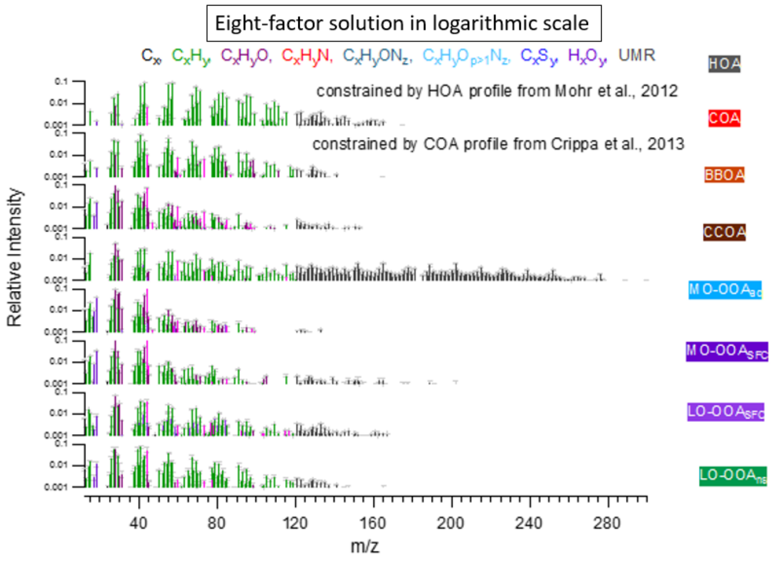

Figure S10. Factor time series, factor profiles in linear scale (top) and logarithmic scale (bottom) of the eight-factor solution from AMS PMF

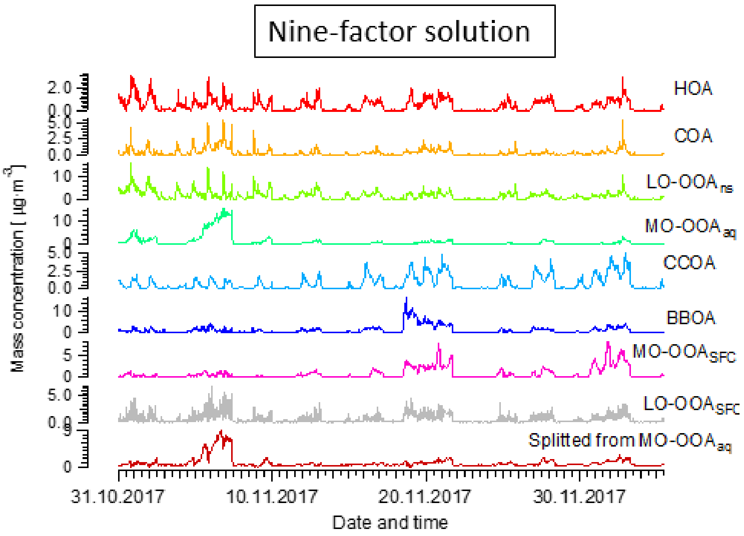

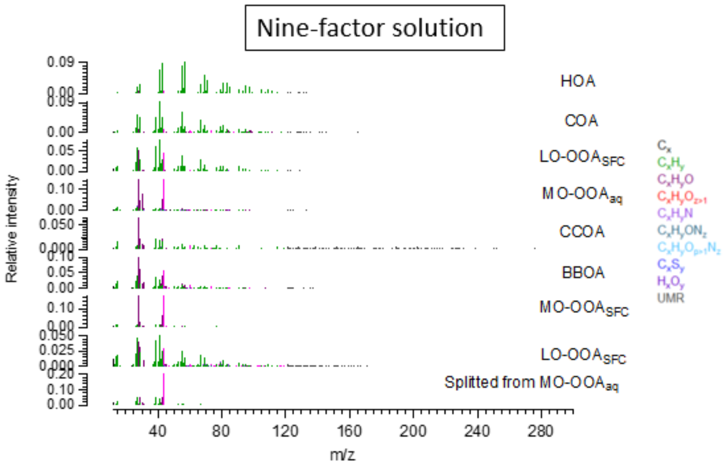

Figure S11. Factor time series, factor profiles of nine-factor solution from AMS

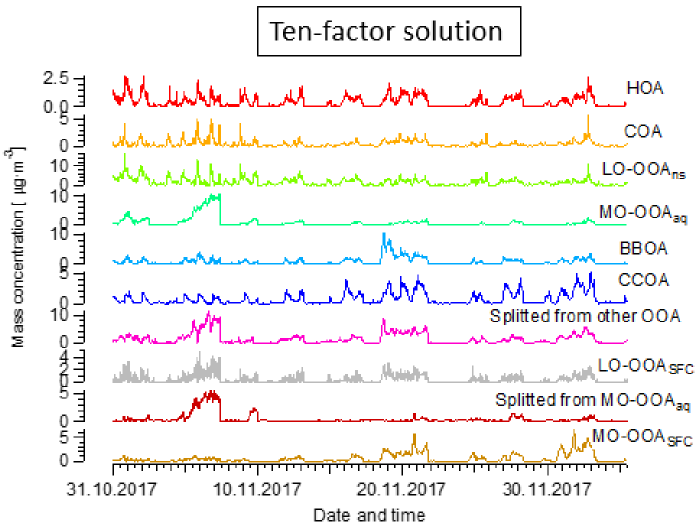

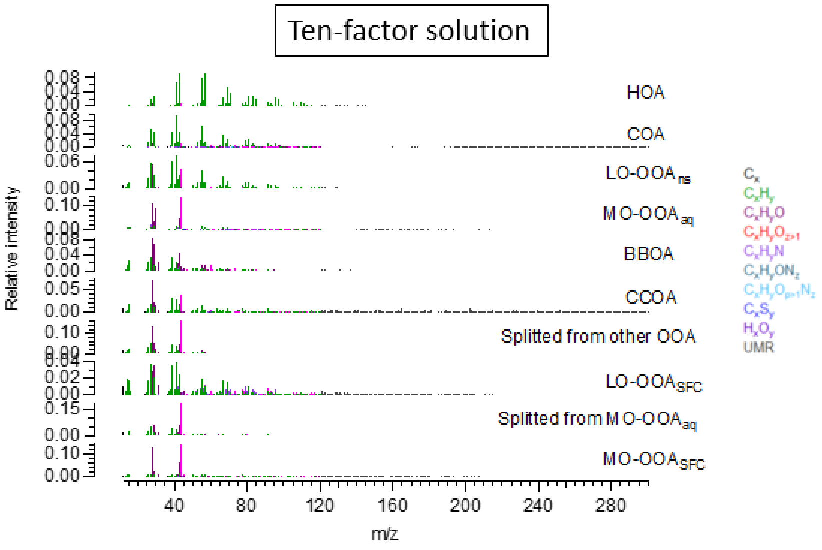

Figure S12. Factor time series and factor profiles of ten-factor solution to ten-factor solution.

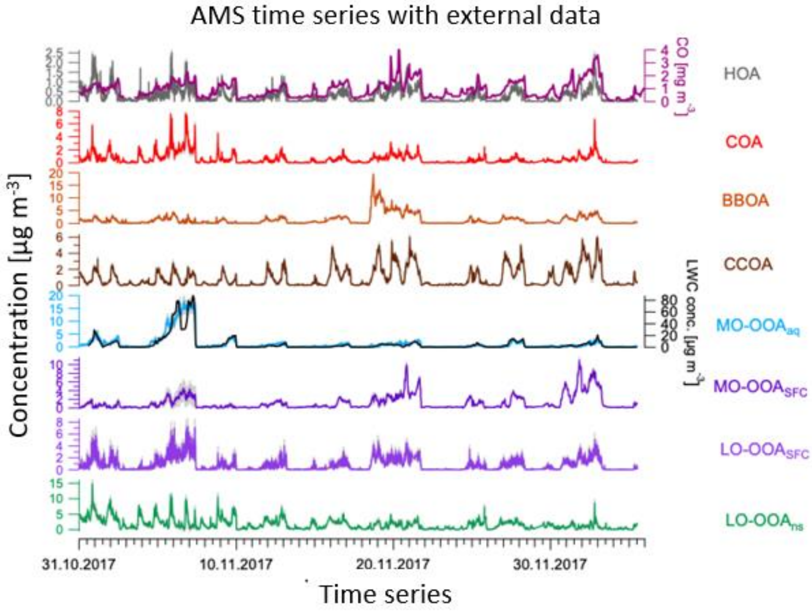

Figure S13. AMS factor time series from the 8-factor solution compared CO and LWC concentration time series.

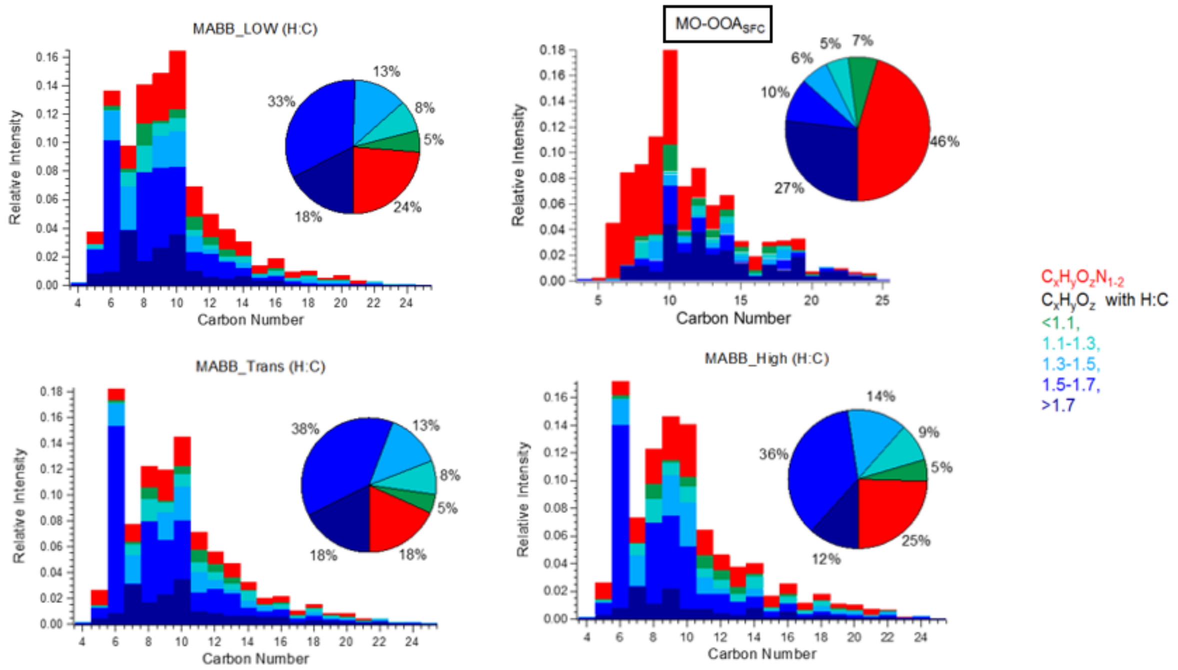

Figure S14. Carbon number distribution of three more-aged biomass burning factors from retrieved from PMF analysis of winter data in Zurich, Switzerland (Qi et al. (2019) compared to MO-OOA$_{SFC}$ (bottom right), coloured by $C_xH_yO_zN_{1-2}$ and five different $C_xH_yO_z$ categories based on H:C ratio (H:C < 1.1, 1.1 < H:C < 1.3, 1.3 < H:C < 1.5, 1.5 < H:C < 1.7 and H:C > 1.7). The sum of each distribution is normalised to 1.

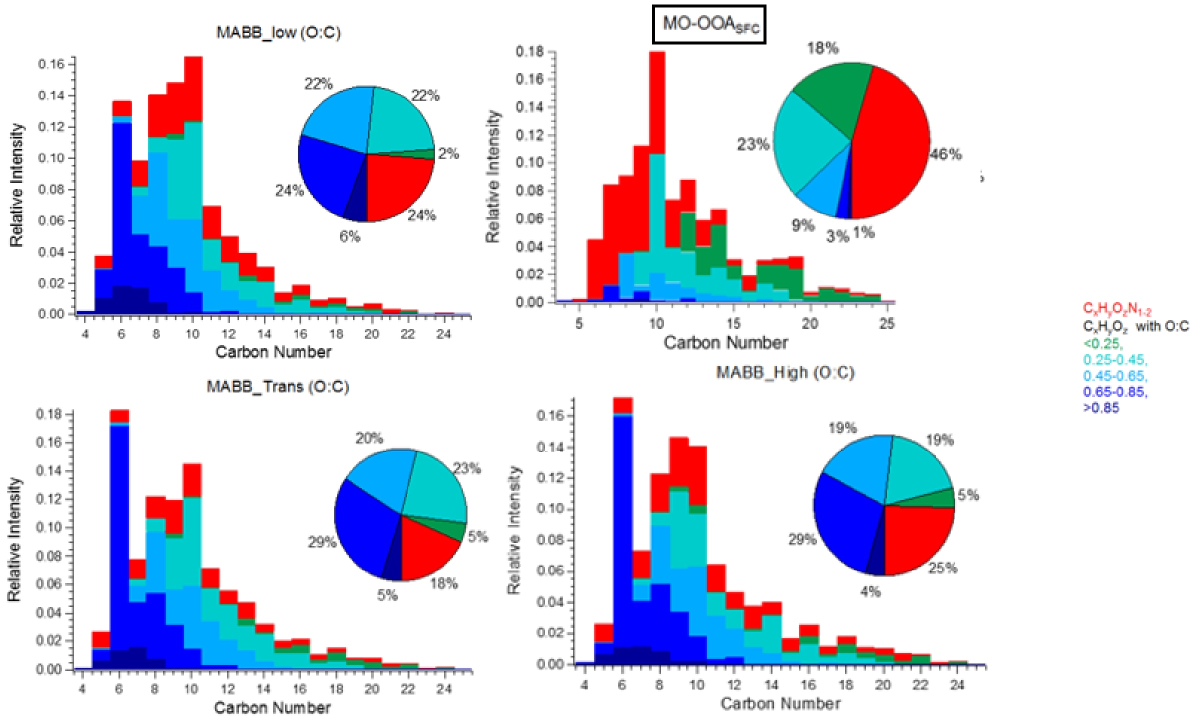

Figure S15. Carbon number distribution of three more-aged biomass burning factors from Qi et al. (2019) compared to $\text{MO-OOA}_{\text{SFC}}$ (bottom right), coloured by $C_xH_yO_zN_{1\text{-}2}$ and five different $C_xH_yO_z$ categories based on O:C ratio (O:C < 0.25, 0.25 < O:C < 0.45, 0.45 < O:C < 0.65, 0.65 < O:C < 0.85 and O:C > 0.85). The sum of each distribution is normalised to 1.

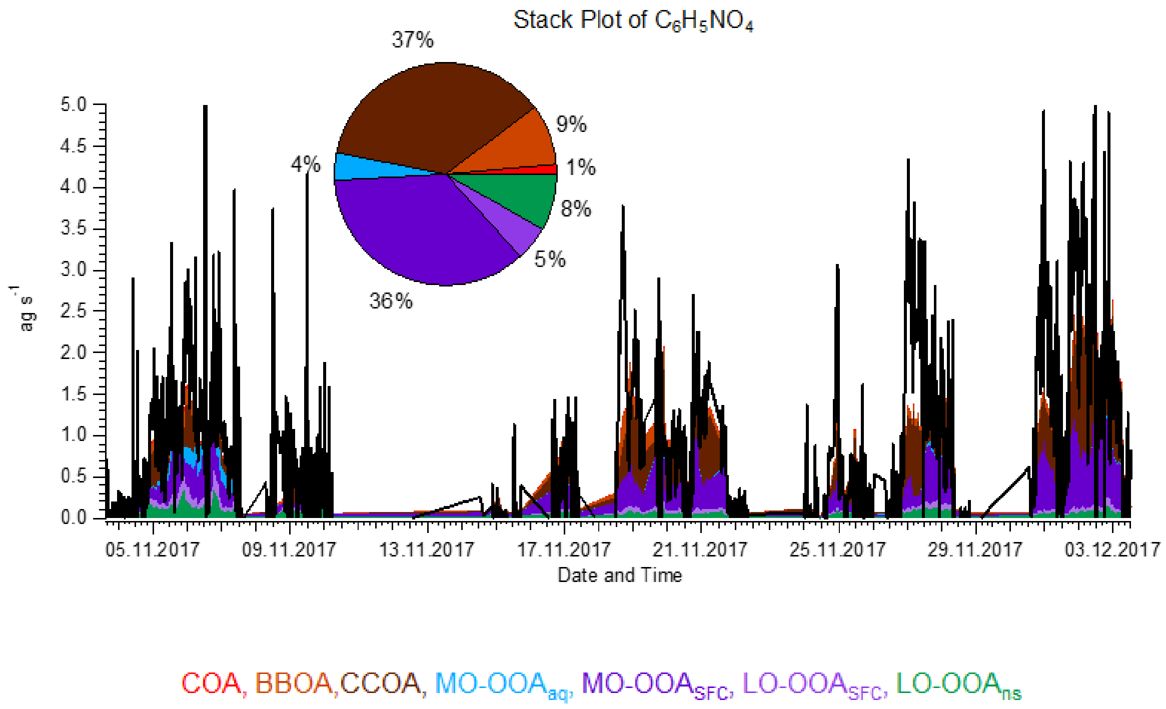

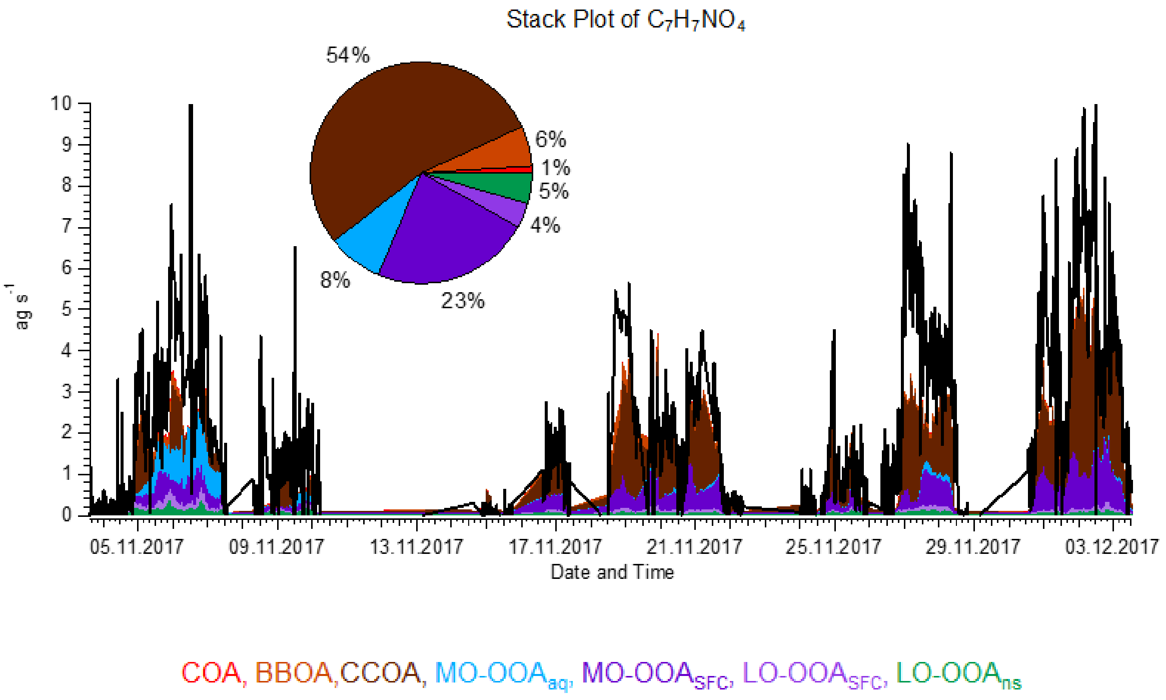

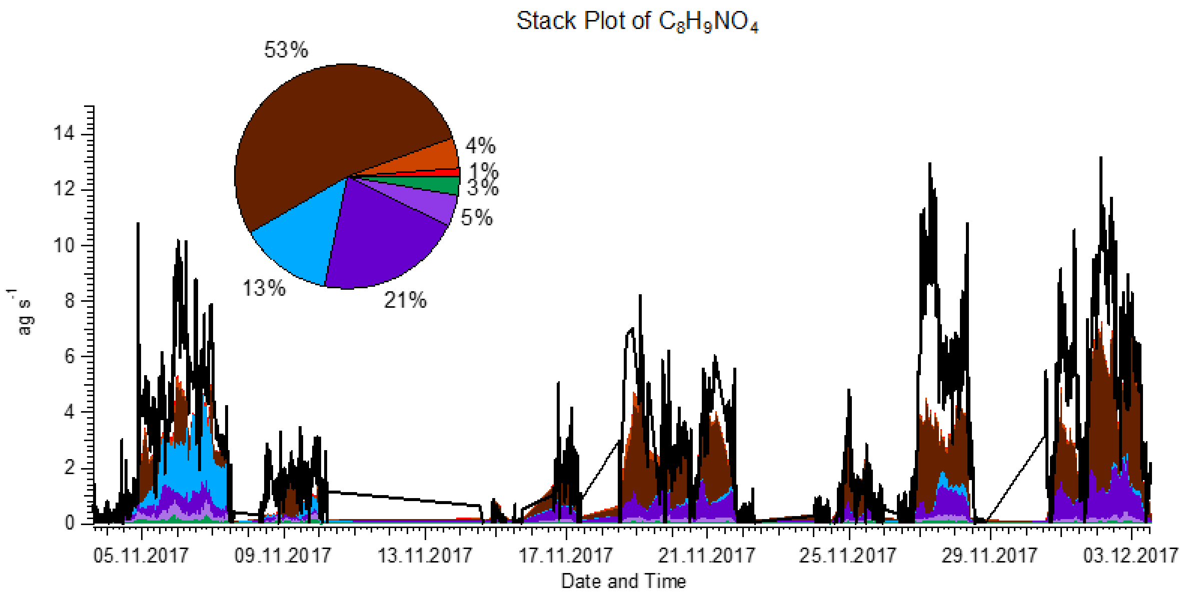

COA, BBOA,CCOA, MO-OOA$_{aq}$, MO-OOA$_{SFC}$, LO-OOA$_{SFC}$, LO-OOA$_{ns}$

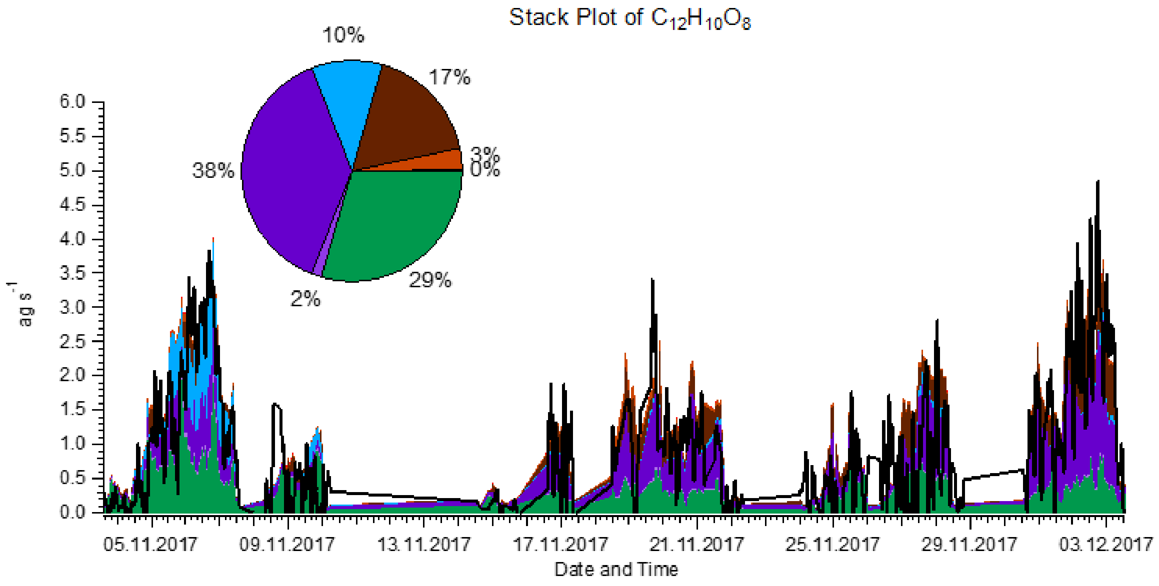

COA, BBOA,CCOA, MO-OOA$_{aq}$, MO-OOA$_{SFC}$, LO-OOA$_{SFC}$, LO-OOA$_{ns}$

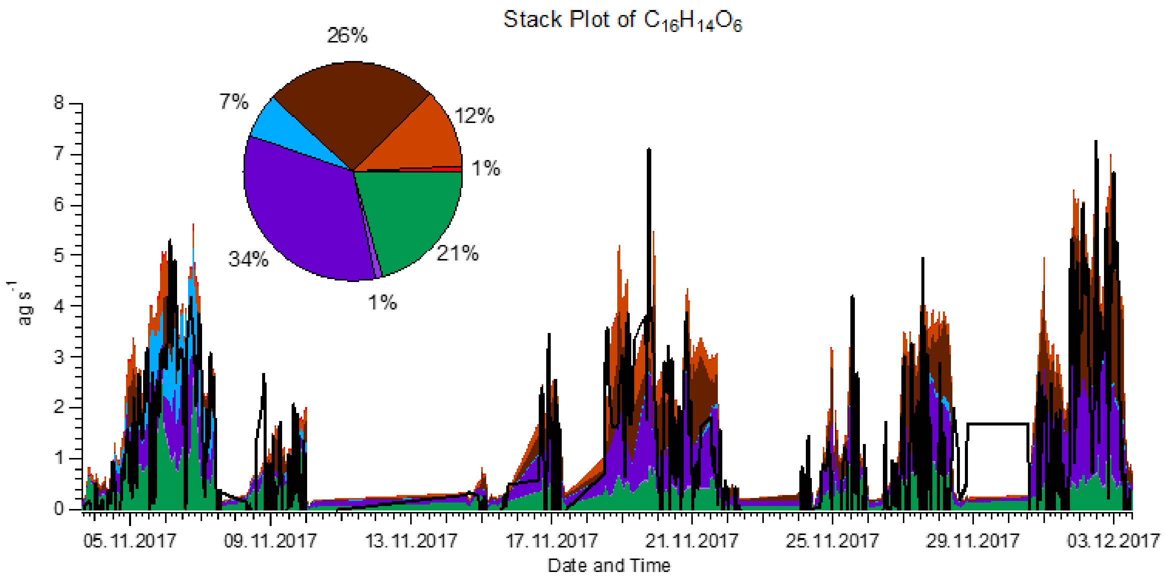

COA, BBOA,CCOA, MO-OOA$_{aq}$, MO-OOA$_{SFC}$, LO-OOA$_{SFC}$, LO-OOA$_{ns}$

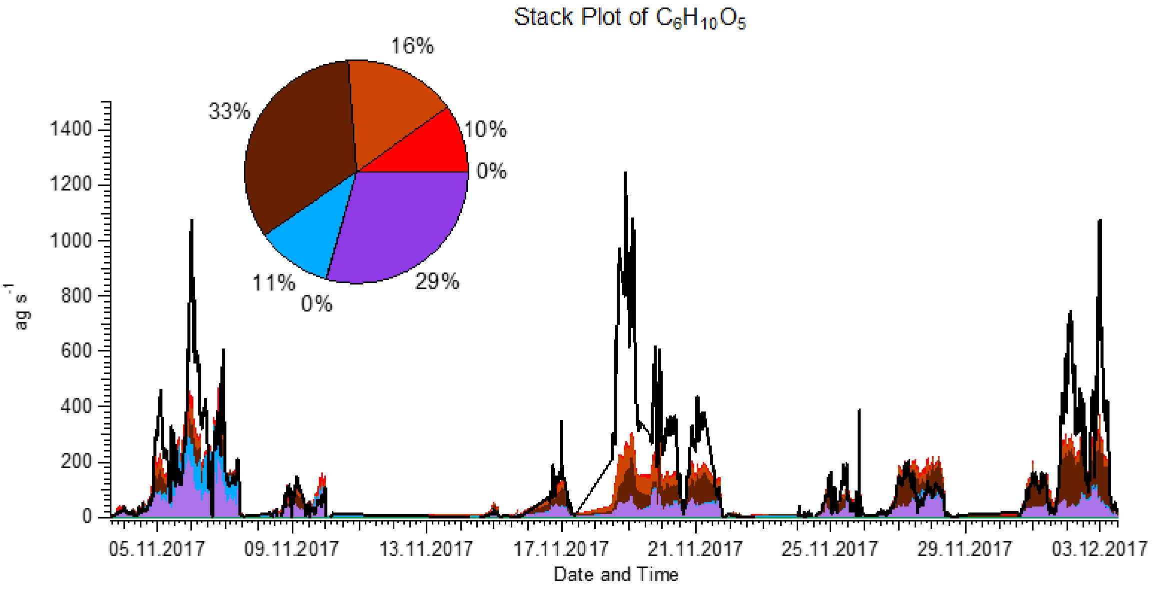

COA, BBOA,CCOA, MO-OOA$_{aq}$, MO-OOA$_{SFC}$, LO-OOA$_{SFC}$, LO-OOA$_{ns}$

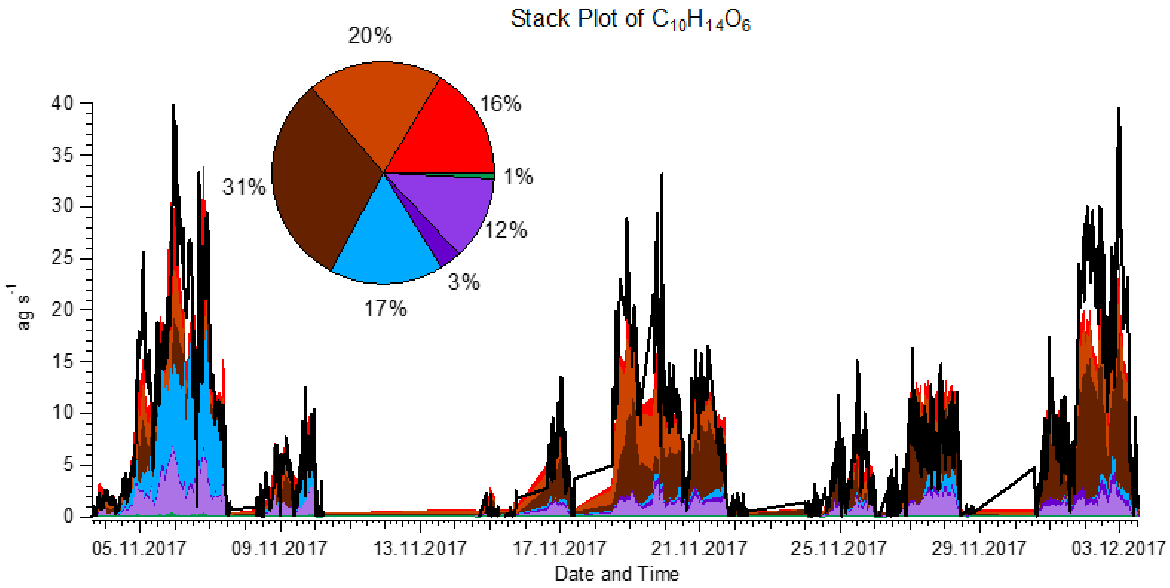

COA, BBOA,CCOA, MO-OOA$_{aq}$, MO-OOA$_{SFC}$, LO-OOA$_{SFC}$, LO-OOA$_{ns}$

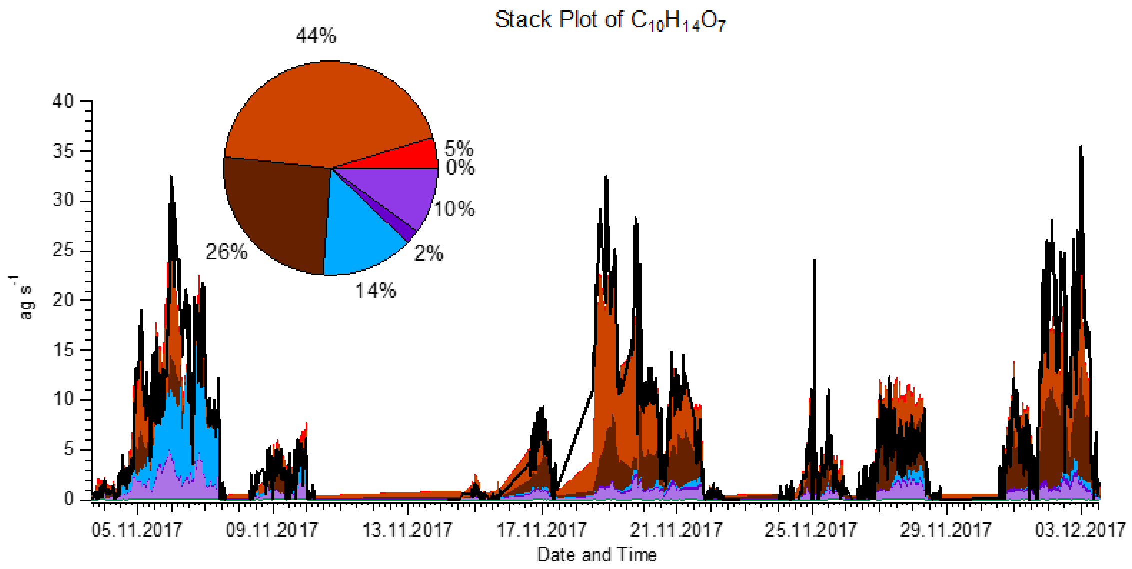

COA, BBOA,CCOA, MO-OOA$_{aq}$, MO-OOA$_{SFC}$, LO-OOA$_{SFC}$, LO-OOA$_{ns}$

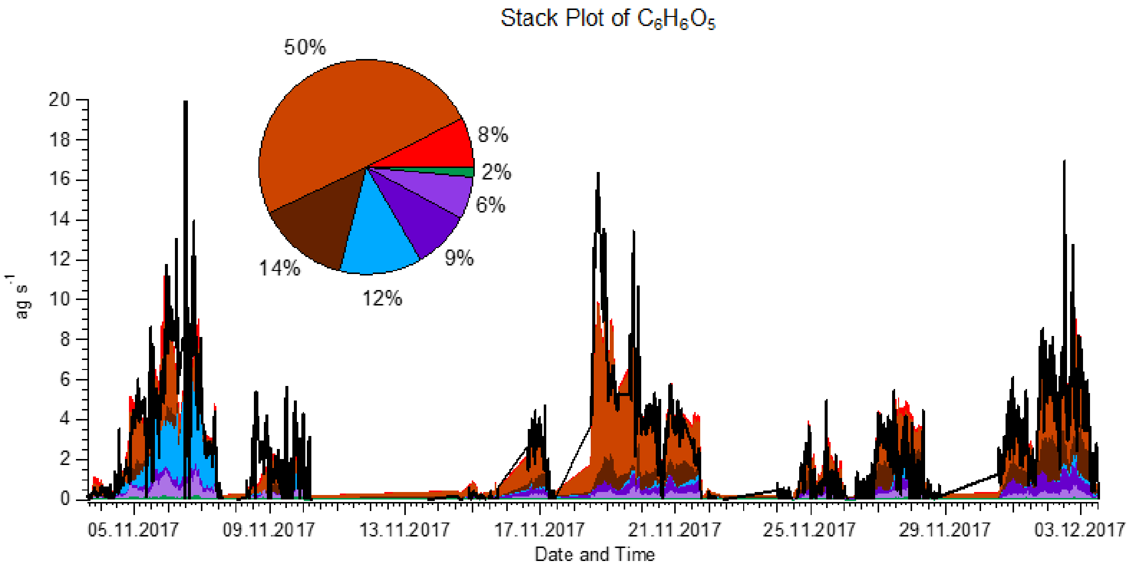

COA, BBOA,CCOA, MO-OOA$_{aq}$, MO-OOA$_{SFC}$, LO-OOA$_{SFC}$, LO-OOA$_{ns}$

Figure S16. Contribution of the resolved factors to the time series of selected ions measured by the EESI-TOF: $C_6H_5NO_4$, $C_7H_7NO_4$, $C_8H_9NO_4$, $C_{12}H_{10}O_8$, $C_{16}H_{14}O_6$, $C_6H_{10}O_5$, $C_{10}H_{14}O_6$ and $C_{10}H_{14}O_7$. Total ion signal is shown as a solid black line, with exceptions for the solid black line for $C_{12}H_{10}O_8$, $C_{16}H_{14}O_6$, which are smoothed by binomial algorithm due to low signal to noise ratio.

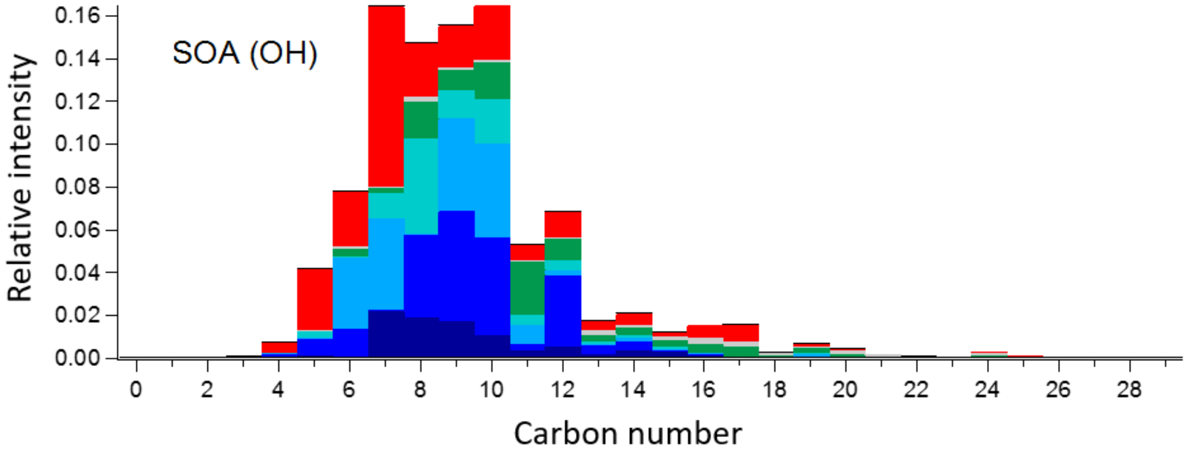

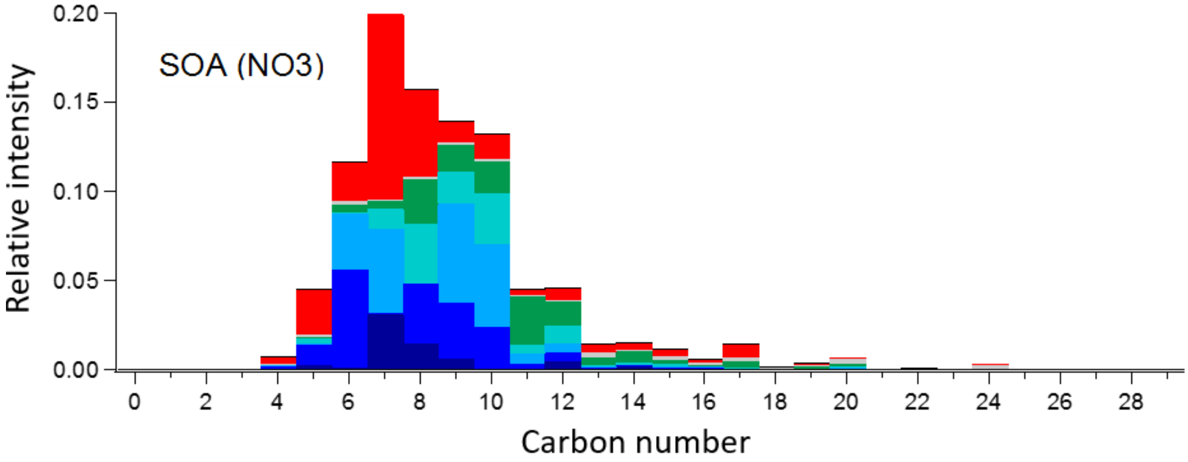

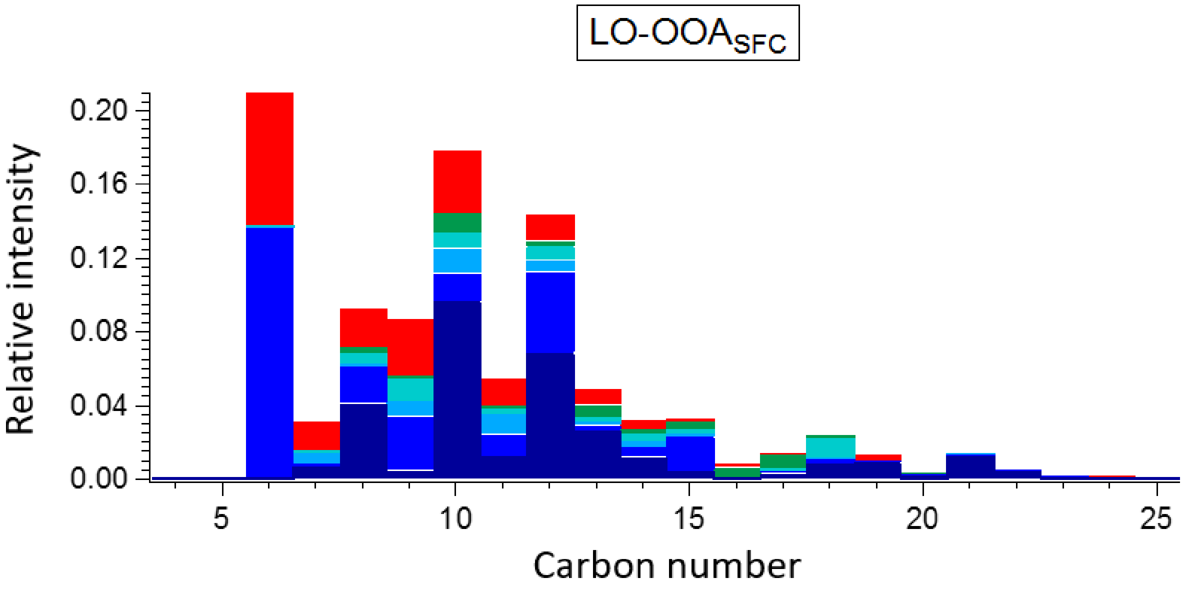

Figure S17. Comparison of carbon number distribution plots by $C_xH_yO_zN_{1-2}$ and five different $C_xH_yO_z$ categories based on H:C ratio (H:C < 1.1, 1.1 < H:C < 1.3, 1.3 < H:C < 1.5, 1.5 < H:C < 1.7 and H:C > 1.7), from wood burning study aged by OH (top) and NO_3 (middle) from Bertrand et al. and LO-OOA$_{SFC}$ from this study (bottom).

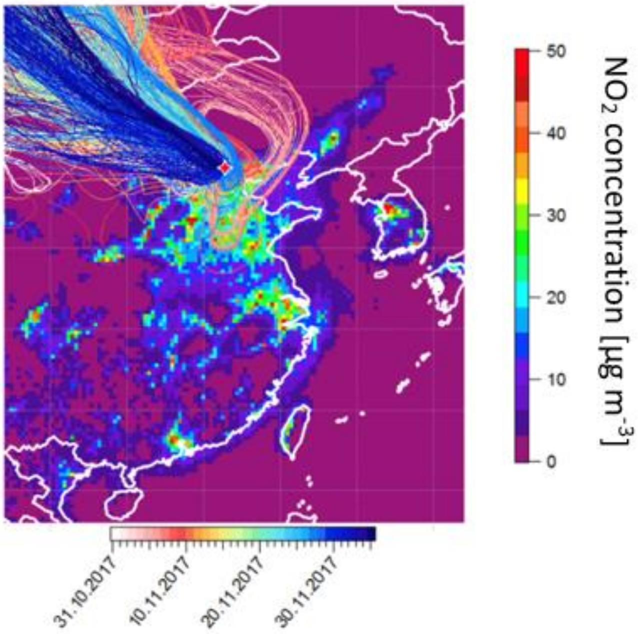

Figure S18. 72h backward trajectory for the whole campaign colour-coded by date and time calculated by Hysplit, overlaid on a 2015 map of surface NO_2 concentrations based on the CHIMERE model and driven by the 2015 DECSO inventory (Liu et al., 2018).

Table S1. List of ions with highest relative intensity and highest z-score in each factor.

Factor Name	Ions with Highest Relative Intensity (Relative Intensity)	Ions with Highest z-score (z-score)
COA	$C_{18}H_{32}O_2$ (0.0957) $C_{21}H_{38}O_3$ (0.0728) $C_{19}H_{36}O_3$ (0.0649) $C_{18}H_{34}O_2$ (0.0572) $C_{10}H_{22}O_3$ (0.0507)	$C_{18}H_{32}O_2$ (1.86) $C_{18}H_{34}O_2$ (1.86) $C_{19}H_{36}O$ (1.83) (only 3 ions with z-core higher than 1.5)
BBOA	$C_6H_{10}O_5$ (0.0659) $C_{10}H_{16}O_4$ (0.0172) $C_9H_{10}N_2O$ (0.0172) $C_8H_{14}O_4$ (0.0159) $C_{17}H_{34}O_3$ (0.0138)	$C_8H_{11}NO_4$ (1.99) $C_{12}H_{16}O_8$ (1.88) $C_8H_{11}NO_7$ (1.87) $C_9H_{12}O_6$ (1.86) $C_7H_{12}O_5$ (1.85)

CCOA	$C_6H_{10}O_5$ (0.0856)	$C_8H_9NO_4$ (2.08)
	$C_{10}H_{22}O_3$ (0.0931)	$C_{11}H_{15}NO_4$ (1.81)
	$C_{10}H_{10}O_3$ (0.0223)	$C_{14}H_{10}O_2$ (1.76)
	$C_{10}H_{14}O_3$ (0.0212)	$C_{12}H_{16}O_3$(1.60)
	$C_{12}H_{22}O_4$ (0.0150)	$C_9H_{11}NO_4$ (1.60)
MO-OOA$_{aq}$	$C_{12}H_{22}O_3$ (0.0581)	$C_9H_{15}NO_6$ (1.79)
	$C_{10}H_{18}O_3$ (0.0415)	$C_{10}H_{17}NO_5$ (1.87)
	$C_6H_{10}O_5$ (0.0286)	$C_8H_{13}NO_6$ (1.75)
	$C_{12}H_{22}O_2$ (0.0254)	$C_9H_{15}NO_5$ (1.92)
	$C_{11}H_{20}O_3$ (0.0210)	$C_9H_{14}O_4$ (1.74)
MO-OOA$_{SFC}$	$C_7H_{13}NO_4$ (0.0314)	$C_6H_9NO_4$ (2.08)
	$C_8H_{15}NO_4$ (0.0270)	$C_6H_{11}NO_4$ (2.09)
	$C_9H_{17}NO_4$ (0.0266)	$C_9H_9NO_2$ (1.92)
	$C_{10}H_{18}O_3$ (0.0241)	$C_7H_{15}NO_4$ (2.22)
	$C_6H_{11}NO_4$ (0.0224)	$C_5H_7NO_6$ (2.12)
LO-OOA$_{SFC}$	$C_6H_{10}O_5$ (0.105)	$C_8H_{16}O_4$ (2.03)
	$C_6H_{11}NO_4$ (0.0523)	$C_{13}H_{20}O_4$ (1.84)
	$C_{10}H_{22}O_3$ (0.0520)	$C_{14}H_{24}O_3$ (1.69)
	$C_8H_{14}O_4$ (0.0275)	(only 3 ions)
	$C_{15}H_{24}O_5$ (0.0244)	
LO-OOA$_{ns}$	$C_{10}H_{22}O_3$ (0.0408)	(no ion with significant z-score)
	$C_{12}H_{22}O_3$ (0.0276)	
	$C_8H_{14}O_4$ (0.0260)	

	$C_8H_{16}O_4$ (0.0255) $C_{12}H_{22}O_2$ (0.0228)	

References

Bertrand, A., Yuan, B., Stefenelli, G., Qi, L., Pospisilova, V., Tong, Y., Sepideh, E., Huang, R. J., El Haddad, I., Slowik, J. G., and Prevot, A.: Characterization of fresh and aged solid fuel combustion organic aerosol by extractive electrospray ionization time-of-flight mass spectrometer (EESI-TOF), in preparation.

Donahue, N. M., Epstein, S. A., Pandis, S. N., and Robinson, A. L.: A two-dimensional volatility basis set: 1. organic-aerosol mixing thermodynamics, Atmos Chem Phys, 11, 3303-3318, https://doi.org/10.5194/acp-11-3303-2011, 2011.

Li, Y., Poschl, U., and Shiraiwa, M.: Molecular corridors and parameterizations of volatility in the chemical evolution of organic aerosols, Atmos Chem Phys, 16, 3327-3344, https://doi.org/10.5194/acp-16-3327-2016, 2016.

Lopez-Hilfiker, F. D., Pospisilova, V., Huang, W., Kalberer, M., Mohr, C., Stefenelli, G., Thornton, J. A., Baltensperger, U., Prevot, A. S. H., and Slowik, J. G.: An extractive electrospray ionization time-of-flight mass spectrometer (EESI-TOF) for online measurement of atmospheric aerosol particles, Atmos Meas Tech, 12, 4867-4886, https://doi.org/10.5194/amt-12-4867-2019, 2019.

Paatero, P., and Hopke, P. K.: Discarding or downweighting high-noise variables in factor analytic models, Anal Chim Acta, 490, 277-289, https://doi.org/10.1016/S0003-2670(02)01643-4, 2003.

Qi, L., Chen, M. D., Stefenelli, G., Pospisilova, V., Tong, Y. D., Bertrand, A., Hueglin, C., Ge, X. L., Baltensperger, U., Prevot, A. S. H., and Slowik, J. G.: Organic aerosol source apportionment in Zurich using an extractive electrospray ionization time-of-flight mass spectrometer (EESI-TOF-MS) - Part 2: Biomass burning influences in winter, Atmos Chem Phys, 19, 8037-8062, https://doi.org/10.5194/acp-19-8037-2019, 2019.

Stefenelli, G., Pospisilova, V., Lopez-Hilfiker, F. D., Daellenbach, K. R., Hüglin, C., Tong, Y., Baltensperger, U., Prévôt, A. S. H., and Slowik, J. G.: Organic aerosol source apportionment in Zurich using an extractive electrospray ionization time-of-flight mass spectrometer (EESI-TOF-MS) – Part 1: Biogenic influences and day–night chemistry in summer, Atmos. Chem. Phys., 19, 14825-14848, https://doi.org/10.5194/acp-19-14825-2019, 2019.